RESEARCH
          Open Access

Performance comparison of a standing-wave thermoacoustic engine with different resonator shapes with air working gas

Zahra Bouramdane[1*] and Abdellah Bah[1]

Abstract

The resonator is one of the key components of thermoacoustic machines and the choice of its geometry is of course of crucial importance, as it determines the way the machine operates. The resonator must be designed so that the quality factor of the resonance is as high as possible and must satisfy the technological production constraints related to the high pressurization of the working fluid and the presence of temperature non-uniformities. The shape of the resonator can be modified to reduce certain loss phenomena, particularly on the walls, and to limit the formation of harmonics in the high-level acoustic field. In this work, an acoustic power losses analysis and a numerical study of a standing-wave TAE with air working gas, considering changes in resonator shape, are performed to investigate the effect of resonator geometry on the thermoacoustic energy conversion. The acoustic power dissipation in the resonator is analyzed based on the simplified thermoacoustic theory and the numerical study is conducted based on a 2D numerical model based on a CFD analysis. Results show that the shape of the resonator significantly affects the frequency, the temperature along the stack, and the acoustic pressure produced on the TAE. In addition, it is shown that the resonator composed of two different diameters showed its ability to produce a high acoustic pressure amplitude (20.5% than the iso-diameter resonator) and minimize the viscous and thermal losses.

Keywords Thermoacoustic engine, Resonator, CFD, Optimization

1 Introduction

Thermoacoustic engines are devices that convert heat into acoustic energy. Unlike most machines, TAEs have no moving parts other than the fluid. The efficiency of these machines is generally lower than those of conventional machines, but they have advantages in implementation and maintenance costs. Thermoacoustic engines consist in their simplest versions of an acoustic resonator inside which placed a stack fitted with heat exchangers at its ends. It is the temperature difference across the stack, maintained by the two heat exchangers, which gives rise

to the acoustic wave amplified by the resonator, which is a key element of TAEs.

Various studies in the literature have been carried out to investigate the role of resonators and the influence of their geometry on the performance of thermoacoustic machines. In 1974, Rott [1] provided the first theoretical study of the influence of shocks in a resonator on the thermoacoustic effect. In 1990, Muzzerall et al. [2] observed strongly nonlinear oscillations in a standing-wave TAE. In 1992, Swift [3], in his study of a large TAE operating at high amplitude, showed that the appearance of corresponding harmonics affects the performance of thermoacoustic devices. In 1993, Gaitan and Atchley [4] showed that the anharmonicity of resonators can be increased by introducing section changes; this means that the resonance frequencies of the different modes are not an integer multiple of the resonance frequency

*Correspondence:
Zahra Bouramdane
zahra.bouramdane@gmail.com
[1] Thermal and Energy Research Team (ERTE), ENSAM, Mohammed V University, Rabat, Morocco

Bouramdane and Bah *Int. J. Air-Cond. Ref.*   (2024) 32:4

Page 2 of 22

associated with the first mode. This anharmonicity is beneficial since it disadvantages the non-linear deformation of an exciting wave in the first mode. Studies by Lawrenson et al. [5], Ilinskii et al. [6], and Chun and Kim [7] as well as by Hamilton et al. [8] focused on anharmonic resonators by modifying their shape and made it possible to obtain very high-intensity acoustic waves with low harmonics. Their studies are conducted in oscillating closed cavities, an acoustical resonator, axisymmetric closed ducts, and an acoustical wave-guide with different cross-sections, respectively. In 2005, Yu et al. [9] conducted a series of experiments to investigate the impact of the resonator length on the characteristics of a TAE having a looped tube and resonator. The experimental results reveal that the resonator length affects the presence of high-frequency mode in the engine. In 2006, Luo et al. [10], Tang et al. [11], and Bao et al. [12] conducted a series of experimental and numerical studies to investigate the effect of the resonator shape on the performance of a traveling-wave TAE by analyzing two different resonators, one resonator is cylindrical, and the other is a tapered one. The experiment and the computed results indicate that the viscous loss in the tapered resonator is much lower than the cylindrical resonator. Xie et al. [13] carried out an experimental study on a thermoacoustic Stirling engine consisting of a looped tube focusing on three axisymmetric types of resonators (cylinder, cone, and cylinder-cone). The results show that the type of resonator influences the pressure waveform and the acoustic field in the system. In 2008, Ueda and Kato [14] conducted a numerical study aiming to explore the stability limits of thermally induced spontaneous gas oscillations in both straight and looped tubes. The findings reveal that the temperature ratio necessary for gas oscillation in looped tubes is influenced by viscosity and the isothermal reversibility of the heat exchange process between the gas and tube wall. Conversely, in straight tubes, the required temperature ratio is determined by the irreversibility of the thermal process. Additionally, the frequency of gas oscillation in straight tubes is contingent on reversibility, whereas in looped tubes, sound speed predominantly influences the oscillation frequency. In 2010, Zink et al. [15] performed a comprehensive CFD analysis on an entire thermoacoustic engine (TAE) to investigate how resonator curvature influences the thermoacoustic effect. The study revealed that the introduction of curvature has a significant impact on the achieved pressure amplitude. Moreover, highly curved resonators displayed variations in operating frequency. In 2012, Hariharan et al. [16] and Qiu et al. [17] conducted an experimental study and numerical simulation to examine how the length of the resonator influences the onset temperature and the overall performance of the thermoacoustic

engine (TAE). The findings indicated that as the resonator length increases, there is a corresponding decrease in working frequency, along with an increase in the onset temperature difference and pressure amplitude. These findings were supported in 2013 by Hariharan et al. [18], who conducted an experimental and simulation studies to explore the effect of resonator length on the performance of twin TAE. In 2013, Muralidharan et al. [19] performed simulation studies employing DeltaEC and CFD analysis to assess the performance of a thermoacoustic prime mover with both straight and conical resonators. In both investigations, the findings revealed that the thermoacoustic prime mover featuring a conical resonator exhibited a higher frequency compared to the iso-diameter resonator. This difference was attributed to increased thermoviscous losses and nonlinear effects in the straight resonator, highlighting the superior performance of the conical resonator. Yang et al. [20] conducted an experimental exploration into the impact of resonator curvature on the thermoacoustic effect and sound energy losses. Their findings indicated that the coiled tube exhibited the highest transmission loss, followed by the U-shaped tube, 90° tube, and finally the straight tube. This observation was corroborated in 2015 by Tourkov et al. [21], affirming the feasibility of designing thermoacoustic devices with bent resonators. In 2017, Cahyadi et al. [22] delved into an experimental study of resonant frequency in a thermoacoustic prime mover, revealing a correlation between the order of resonant frequencies and the length of the resonator. Extending the resonator length, as shown, decreased the resonant frequency while increasing the viscous penetration depth. Further studies in 2018 by Yang et al. [23] employed an optimization method based on gradient derivation, focusing on the acoustic damping of multiple Helmholtz resonators attached to a thin annular duct. Bourquard and Noiray [24] conducted an experimental and theoretical investigation, centering on the stabilization of acoustic modes using Helmholtz and quarter-wave resonators. Their results emphasized the achievement of optimal stabilization at an exceptional point for tuned dampers. In 2018, our group utilized CFD simulation to explore the impact of resonator curvature and the length alteration with a constant curvature angle on the thermoacoustic process [25]. The results highlighted the resonance frequency and acoustic pressure level being affected by the resonator bend. Balonji et al. [26] in 2019 conducted a numerical study showcasing the potential of regulating TAE performance by adjusting resonator geometry. Their evaluation revealed that altering the resonator length influenced start-up temperature, resonant frequency, acoustic power, and thermal efficiency. Harikumar et al. [27] undertook an experimental study on thermoacoustic

Bouramdane and Bah *Int. J. Air-Cond. Ref.*   (2024) 32:4

Page 3 of 22

energy conversion in a square duct using a plastic straw as a stack. This study provided a qualitative insight, demonstrating that a significant temperature difference could be achieved using a square resonator.

The majority of numerical studies on acoustic propagation in resonators have predominantly focused on straight geometries. The impact of resonator geometry in unconventional configurations on the conversion of thermal energy into acoustic energy in standing-wave thermoacoustic engines (TAEs) has received comparatively little attention. While this approach avoids the need to simulate lengthy ducts or intricate geometries, it comes with the drawback of increased numerical calculation expenses, as these geometries significantly widen the bandwidth of matrices in finite element calculations. Further research is essential to unveil the intricate relationship between resonator shape and the performance of these machines. In this study, we conduct an analysis of acoustic power losses and employ a two-dimensional numerical model based on CFD simulation. The goal is to simulate and scrutinize the evolution of the self-excited process of thermoacoustic oscillations with various resonator shapes, shedding light on how resonator geometry influences the performance of standing-wave TAEs. Five distinct resonator shapes are under examination, including a straight resonator with an adjusted length, outwardly and inwardly tapered resonators, a curved resonator, and a model featuring a resonator composed of two sections with different diameters separated by a conical section. The self-excited process, spanning from the initial disturbance to the steady state of the acoustic wave generated by the engine, is analyzed in each case. Conclusive results encompassing the amplitude of the acoustic pressure, frequency, temperature along the resonator length, and sound pressure level are presented and discussed.

2 Resonator in standing-wave thermoacoustic machines

In thermoacoustic devices, the resonator material plays a critical role, necessitating careful consideration of its acoustical, mechanical, and thermal properties. The material must exhibit sufficient strength to withstand the operating pressure and impermeability, especially when using helium as the working fluid. To ensure optimal efficiency, it is crucial to minimize thermal and viscous losses at the resonator's interior walls. The choice of resonator material involves three key factors: mechanical strength, acoustics, and heat transfer. Mechanically, the material must be robust and impermeable, particularly when dealing with high pressures. Acoustically, the material should have a large impedance, treating the working gas as a rigid boundary to minimize losses

in acoustic wave pressure. Dense materials, like metals, exhibit high characteristic impedance, making them suitable for acoustic resonators. Additionally, metals possess excellent strength-to-weight ratios, making them ideal for pressure vessels. However, using metals as resonator materials in thermoacoustic applications presents challenges. Metals with high thermal conductivities facilitate heat transfer between ambient temperature and the cold side of the resonator. Heat leakage in the cold side necessitates using some of the stack's cooling power to move the heat across the stack, resulting in energy wastage. Therefore, it is advisable to choose a material with low thermal conductivity for the resonator. For efficient performance, the resonator should allow good thermal contact between the gas in the cold end and the cold end of the stack, enabling a rapid attainment of the steady state. A material with high thermal conductivity is desirable on the interior of the resonator away from the stack to facilitate faster heat flow through the wall, maintaining temperature uniformity away from the stack. However, around the stack, the resonator should exhibit very low thermal conductivity, even on the interior walls, to prevent heat leakage from the hot side back to the cold side. In summary, an ideal resonator material should have a low overall thermal conductivity for effective thermoacoustic performance.

Figure 1 presents two possible geometries of a standing-wave resonator. A standing-wave resonator can be a half or a quarter-wavelength. A half-wavelength resonator (Fig. 1a) is simply a tube closed at both ends so that the velocity vanishes at the endpoints. A quarter-wavelength resonator (Fig. 1b) is half as long but still resonates at the same frequency because the end away from the driver is open where the pressure is zero, but the velocity is a maximum. It turns out that geometry (c) is much
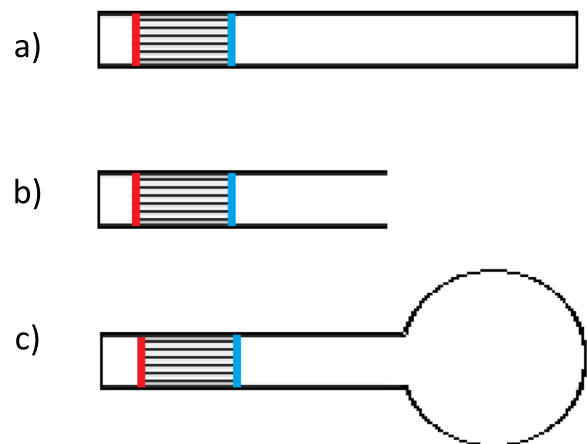

Fig. 1 Different geometry of a standing-wave resonator

Bouramdane and Bah *Int. J. Air-Cond. Ref.* (2024) 32:4

Page 4 of 22

preferable to the classic geometry (a and b) for several reasons. For the same operating frequency, geometry (c) is more compact than geometry (a and b). In other words, a Helmholtz resonator resonating at 100 Hz is shorter than a quarter-wave resonator resonating at the same frequency and the quality factor associated with acoustic resonance is higher for the waveguide buffer volume than for the straight resonator.

3 Acoustic power dissipation in the resonator

Resonator losses are due to viscous dissipation and thermal relaxation along the wall in the boundary layer, defined by the viscous and thermal penetration depths. In general, shorter/smaller resonators are better for thermoacoustic applications as they have fewer losses. Assuming that all dimensions of the resonator are much larger than the penetration depths and that the temperature gradient along the axis of the resonator is zero, the acoustic power loss per unit area in a half-wavelength resonator is estimated as follows [28]:

$$\frac{dW_{loss}}{dS} = -\frac{1}{4}\rho_m \left|\frac{u}{A_g}\right|^2 \delta_\nu \omega - \frac{1}{4}\frac{|p|^2}{\gamma p_m}(\gamma - 1)\delta_k \omega \quad (1)$$

where δ_k is the thermal penetration depth, δ_ν is the viscous penetration depth, ω is the angular frequency, p is the pressure, and u is the gas velocity, given by:

$$p = P_A \cos(kx) \quad (2)$$

$$u = \frac{P_A}{\rho_m a}\sin(kx) \quad (3)$$

$$\delta_k = \sqrt{\frac{2K}{\rho C_{p\omega}}} \quad (4)$$

$$\delta_\nu = \sqrt{\frac{2\mu}{\rho\omega}} \quad (5)$$

Equation (1) indicates that there are different sets of independent parameters that play an important role in the dissipation of acoustic power in the resonator. Olson and Swift [29] proposed to normalize the acoustic power by the product ($p_m aA$) of the mean pressure p_m, the speed of sound a, and the stack cross-section A. The normalized acoustic power dissipated in a half-wavelength resonator is estimated as follows:

$$W_{rn} \approx -\left[\frac{\pi}{8\gamma}\sqrt{Pr}DR^2\left(\frac{\delta_k}{r_{hr}}\right)\right] - \left[\frac{(\gamma - 1)\pi}{8\gamma}DR^2\left(\frac{\delta_k}{r_{hr}}\right)\right] \quad (6)$$

where r_{hr} is the hydraulic radius of the resonator, Pr is the Prandtl number (defined as the ratio between the viscous boundary layer and the thermal boundary layer), DR is the drive ratio (defined as the ratio of the mean pressure p_m and the pressure amplitude at the pressure antinode). The Pr and DR are given by:

$$Pr = \frac{\mu c_p}{k} = \frac{\upsilon}{\alpha} = \left(\frac{\delta_\nu}{\delta_k}\right)^2 \quad (7)$$

$$DR = \frac{p_0}{p_m} \quad (8)$$

The energy dissipated in the resonator is proportional to the area of the resonator wall. Thus, to determine the normalized sound power dissipated in a quarter-wavelength resonator, the above equation must be divided by two:

$$W_{rn} \approx -\frac{1}{2} \times \left[\frac{\pi}{8\gamma}\sqrt{Pr}DR^2\left(\frac{\delta_k}{r_{hr}}\right)\right] - \frac{1}{2} \times \left[\frac{(\gamma - 1)\pi}{8\gamma}DR^2\left(\frac{\delta_k}{r_{hr}}\right)\right] \quad (9)$$

Equation (9) comprises two terms representing viscous losses and thermal losses. Viscous losses stem from shear forces in the working gas dissipating kinetic energy, while thermal losses result from thermal relaxation in the boundary layer. In Fig. 2, the energy dissipation in the resonator (W_{loss}) is depicted concerning the drive ratio (DR), Prandtl number (Pr), and thermal penetration depth (δ_k) for various resonator diameters (r). The figure illustrates that W_{loss} increases with larger resonator radius and elevated values of DR, Pr, and δ_k. Examining Eq. (9), it becomes evident that the cumulative impact of these loss mechanisms is directly proportional to the resonator's surface area. Consequently, a reduction in the surface area enhances system efficiency. Two approaches exist to minimize the surface area of a standing-wave thermoacoustic resonator. Firstly, adopting the quarter-wavelength resonator geometry proves effective, and secondly, reducing the resonator diameter at the cold end of the stack achieves similar results.

A decrease in the resonator area corresponds to an enhancement in performance. Specifically, a $\lambda/4$ resonator dissipates only half the energy of a $\lambda/2$ resonator. The $\lambda/4$ resonator can undergo additional optimization by diminishing the diameter of the section to the right of the stack, as depicted in Fig. 3. This illustration reveals two distinct parts: a large-diameter tube housing the stack (diameter d_1) and a smaller-diameter tube with diameter d_2. The transition between the large- and small-diameter tubes is denoted by subscript A, while the transition between the small-diameter tube and the buffer volume is denoted by subscript B. In the context
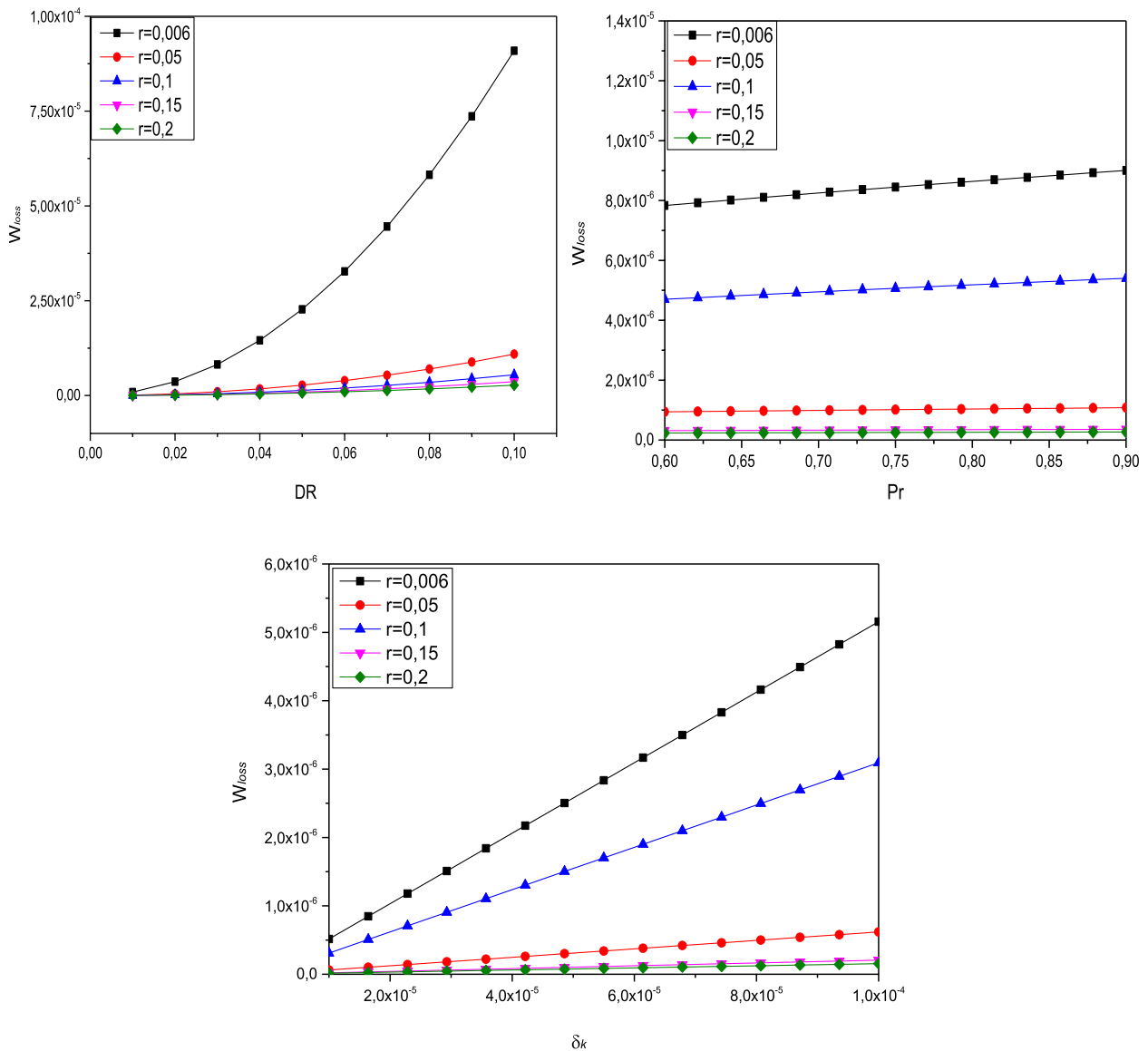
Bouramdane and Bah *Int. J. Air-Cond. Ref.*   (2024) 32:4

Page 5 of 22

Fig. 2 The dissipated energy (W_{loss}) as a function of *DR*, *Pr*, and δ_k for different diameters
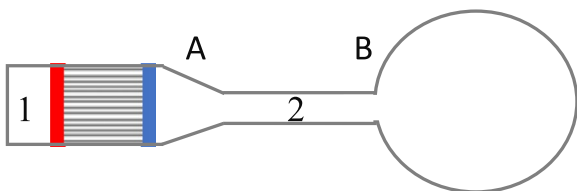

Fig. 3 The optimized resonator to minimize losses per unit area

of a quarter-wavelength resonator, the open end cannot contain pressures exceeding 1 atm. Thus, this end requires simulation with a closed buffer volume as the boundary condition. Consequently, the resonator

length falls between a quarter and half wavelength. By employing a sufficiently large volume, the resonator becomes slightly longer than a quarter wavelength but significantly shorter than a half wavelength. This design minimizes the total surface area of the resonator. Further reduction in the resonator area involves diminishing the diameter of the resonator section between the cold end of the stack and the buffer volume. Maintaining the desired operating frequency necessitates a concurrent reduction in the length of this resonator section, further minimizing the overall surface area. For a resonator consisting of two different diameters, Eq. (1) normalizing by the parameter *N* becomes [29]:

Bouramdane and Bah *Int. J. Air-Cond. Ref.*   (2024) 32:4

Page 6 of 22

$$\frac{W_{loss}}{N} = \frac{d_2}{d_1}\left(\frac{P_2}{P_1}\right)^2\left[\left(1+\frac{\gamma-1}{\sqrt{Pr}}\right)k(x_{B'}-x_{A'}) + \frac{1}{2}\left(1-\frac{\gamma-1}{\sqrt{Pr}}\right)(\sin(2kx_{A'})-\sin(2kx_{B'}))\right] \tag{10}$$

where N is defined as:

$$N = \frac{\pi d_1 \delta_v a p_1^2}{8\gamma P_m} \tag{11}$$

The normalization constant, N, is derived from the losses in the large-diameter tube.

Equation (10) can be plotted for different resonator diameter ratios, as shown in Fig. 4. The red curve represents the thermal losses, the blue curve represents the viscous losses, and the black curve is the sum of the total losses. The heat loss increases monotonically with the ratio d_2/d_1, but the viscous losses decrease rapidly until about $d_2/d_1 = 0.6$ and then increase slowly. As a result, the total loss shows a minimum at $d_2/d_1 = 0.65$.

4 CFD simulation

CFD has evolved from a mathematical curiosity to an indispensable tool in various fluid dynamics disciplines. In research, it stands as a focal point, offering access to instantaneous information (velocity, pressure, concentration, etc.) at every point within the calculation domain. This is achieved at a generally lower global cost compared to corresponding experimental approaches. Despite its merits, the precise prediction of complex phenomena

remains a persistent challenge. Continuous efforts are directed toward the development and enhancement of simulation software. In addition to prevalent commercial CFD tools, the growing popularity of COMSOL Multiphysics is noteworthy, particularly for research applications. As a commercial solver and simulation software founded on the finite element method, COMSOL Multiphysics excels in solving time-dependent equation systems with associated boundary and initial conditions. Details of this software are given in the reference [30].

4.1 Model space

In the context of this study, only resonators comprised of two parallel plates of finite length along the main axis of the resonator and infinite dimension perpendicular to this axis are modeled. This assumption facilitates the use of a two-dimensional model to depict the resonator's behavior.

The reference sample in the model space is a quarter-wavelength standing-wave engine filled with air as the working fluid. The resonator is closed on the left side and open on the right side, measuring $Lr = 150$ mm in length and $l = 12$ mm in width. The stack, composed of parallel plates 10 mm in length and spaced 0.5 mm apart, is positioned 30 mm from the closed end. Figure 5 illustrates
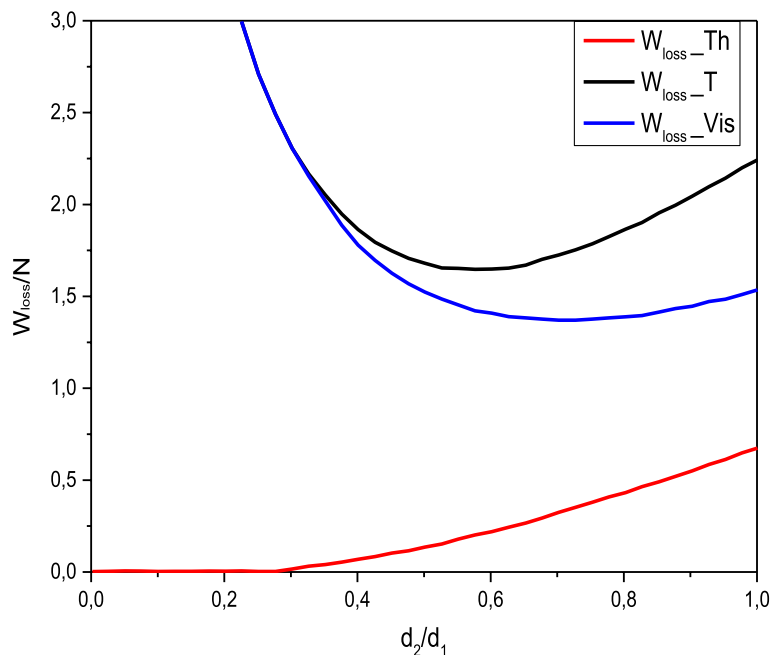

Fig. 4 The losses in the small diameter part of the resonator as a function of d_2/d_1
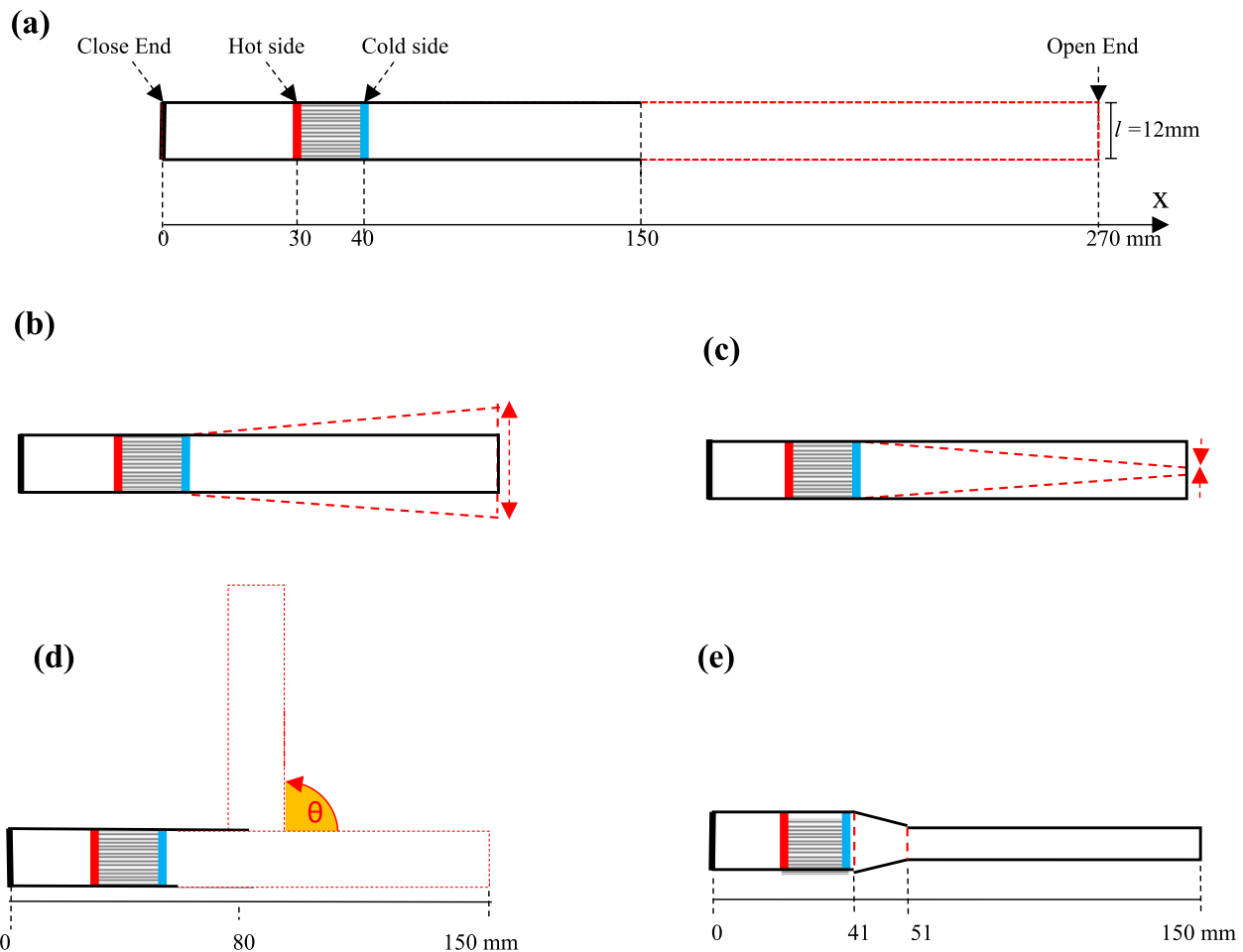
Fig. 5 The schematic diagram of the standing-wave TAE with different **a** resonator lengths, **b** tapered resonators, **c** narrowed resonator, **d** curved resonators, and **e** resonators with two diameters

the computational domains utilized in this study. Model spaces adapted for investigating the impact of different resonator shapes are presented in Fig. 5. For all the considered shapes, the total length, location, thickness, and gap of the plates are kept constant, ensuring a better comparison of results across each case. To explore the effect of different resonator geometries on the thermoacoustic profile, five numerical models are conducted. The first focuses on a straight resonator with an adjusted length ranging from 120 to 270 mm (Fig. 5a). The second considers an outwardly tapered resonator, achieved by extending the open end from 12 to 26 mm (Fig. 5b). The third examines an inwardly tapered resonator, achieved by narrowing the open end from 12 to 2 mm (Fig. 5c). The fourth model investigates the effect of resonator curvature by modeling resonators with various bend angles from $\Theta = 0°$ to $\Theta = 90°$ (Fig. 5d). Lastly, the fifth model explores a resonator composed of two sections with different diameters separated by a conical section of 10 mm.

The section containing the stack remains constant, while the diameter of the ambient side varies from 12 to 2 mm (Fig. 5e).

4.2 Grid dependency

The inherent trade-off between cell size and computational time becomes apparent, where an increased number of constitutive equations requiring iterative solutions extend the simulation process. Moreover, adopting a coarse grid introduces numerical inaccuracies. In thermoacoustic systems, the resonator length is the largest scale, while the viscous thickness ($\delta \nu$) represents the smallest scale. Achieving a robust resolution of the viscous boundary layer demands a substantial number of computational points per viscous thickness, especially in the vicinity of the parallel plates constituting the stack. To determine the optimal mesh size, eight different meshes were generated to scrutinize the results' dependency on mesh properties (Fig. 6). Figure 7 illustrates the evolution
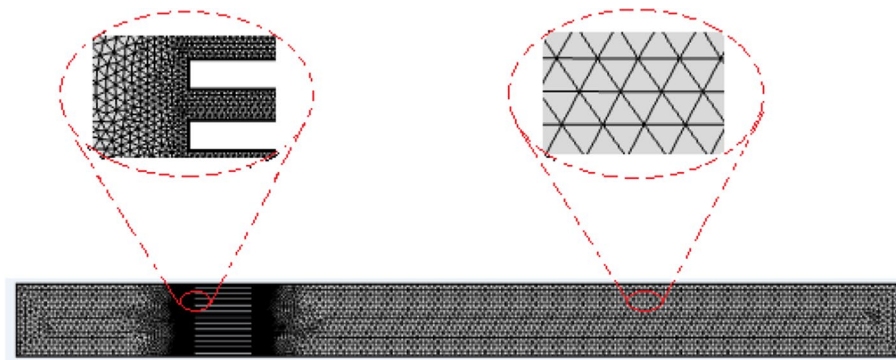
Bouramdane and Bah *Int. J. Air-Cond. Ref.*   (2024) 32:4

Page 8 of 22

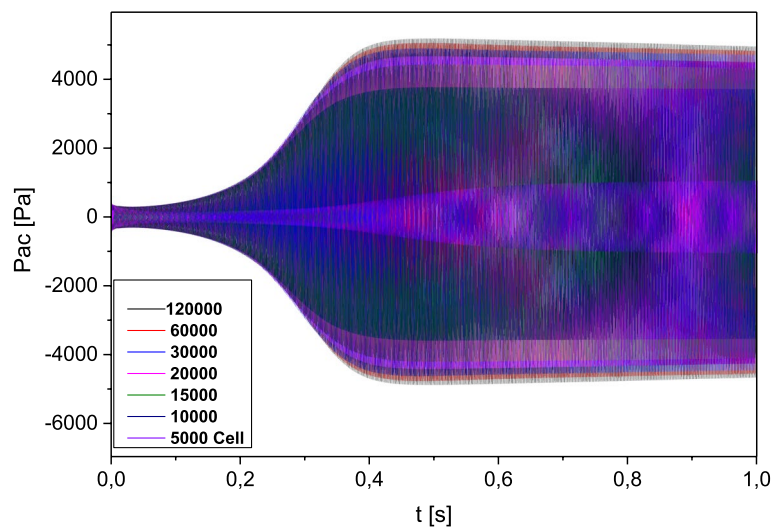**Fig. 6** Refined and relaxed mesh used for the CFD simulation

Fig. 7 Sound pressure (P_{ac}) as a function of mesh properties

of the acoustic pressure at the pressure antinode in the thermoacoustic engine's resonator. A refinement of 5000 cells yields oscillations at a frequency of 585 Hz and a sound pressure amplitude of 1059 Pa. Further refinements, ranging from 10,000 to 20,000 cells, result in an incremental increase in sound pressure amplitude. Notably, the difference between the 60,000-cell grid and the 120,000-cell grid is much smaller than that between the 30,000-cell grid and the 60,000-cell grid. Grid independence, with a difference of approximately 2.5%, is thus achieved at 60,000 cells [31]. For the present simulations, a 30,000-cell triangular mesh is employed (Fig. 6).

4.3 Governing equations

The acoustic variables utilized to characterize the fluid dynamics within the stack and resonator encompass pressure (p), particle velocity (v), density (ρ), and temperature (T). These variables find their expressions in fundamental equations that govern acoustic motion in viscothermal fluid. The key equations involved include the Navier–Stokes equation, conservation of mass equation, heat conduction equation, and the requisite state equations. Through these formulations, a comprehensive understanding of the acoustic behavior in the fluid medium is achieved. These equations can be articulated as follows [32, 33]:

– Mass conservation:

$$\frac{\partial \rho'}{\partial t} + \overrightarrow{\nabla}.\left(\rho_0 \overrightarrow{u}\right) = 0 \tag{12}$$

– Momentum conservation:

$$\rho_0 \frac{\partial \overrightarrow{u}}{\partial t} = -\overrightarrow{\nabla}_p + \mu\left(\overrightarrow{\nabla}\right)^2 \overrightarrow{u} + \left(\eta + \frac{\mu}{3}\right)\overrightarrow{\nabla}.(\overrightarrow{\nabla}.\overrightarrow{u}) \tag{13}$$

– Energy conservation:

$$\rho C_P \left(\frac{\partial T}{\partial t} + u.\nabla T \right) = \nabla.(k\nabla T) + Q_{vh} + W_P \qquad (14)$$

where W_p is the pressure work and Q_{vh} is the involvement of viscous heating process given by:

$$W_P = \alpha_P T \left(\frac{\partial P}{\partial t} \right) \qquad (15)$$

$$Q_{vh} = \tau : \nabla u \qquad (16)$$

In order to establish a connection between the physical parameters of the fluid and address the system of equations delineated earlier, the assumption is made that the working gas adheres to the characteristics of an ideal gas. This assumption is encapsulated in the equation of state, expressed as:

$$\rho = \frac{P}{R_s T} \qquad (17)$$

Finally, the unsteady heat conduction equation for the solid is written:

$$\frac{\partial T}{\partial t} = \alpha \nabla^2 T \qquad (18)$$

Here, α represents the thermal diffusivity of the stack walls, defined as the ratio of the coefficient of thermal conductivity to the density and the specific heat at constant pressure ($\alpha = k/\rho cp$).

4.4 Initial and boundary conditions

In the present simulations, the resonator boundaries act as adiabatic walls, with the exception of the open end, where a temperature of 300 K is imposed. The heat transfer coefficient between plates and the working gas is fixed at 50 W/(m²K). For a comprehensive understanding of each boundary condition pertinent to this study, Fig. 8 depicts various boundaries within the simulation domain. The specified initial conditions and boundary conditions for this study are outlined below:

$$\text{At } t = 0 \text{ at all } x \text{ and } y \text{ cells} \begin{cases} u = 0 \\ v = 0 \\ T = T_m \end{cases} \qquad (19)$$

$$\text{At the closed end} \begin{cases} u = 0 \\ v = 0 \\ \frac{dT}{dx} = 0 \end{cases} \qquad (20)$$

$$\text{Fluid symmetrical boundaries} \begin{cases} \frac{du}{dy} = 0 \\ v = 0 \\ \frac{dT}{dy} = 0 \end{cases} \qquad (21)$$

$$\text{PS surfaces} \begin{cases} u = 0 \\ v = 0 \\ T(x) = 1100 - (500 + 300\cos(\frac{x}{L_{st}})) \end{cases} \qquad (22)$$

The temperature distribution applied to the horizontal walls of the plates creates a gradient, with the hot side of the stack ($x = 0.03$ m) set at 900 K and gradually decreasing along the plate's length to 300 K on the cold side ($x = 0.04$ m). Establishing an initial distribution of flow field factors is vital for dynamic simulations of this nature. In the initial phase of the simulation, a pressure pulse is introduced into the stationary solution, incorporating a smaller time step for the energy equation. This ensures that the pressure distribution along the resonator mirrors the acoustic pressure oscillations, while the temperature gradient remains unchanged. Figure 9 illustrates the distributions of pressure and velocity fields along the thermoacoustic engine. Notably, the pressure decreases from the hot side to the cold side of the stack, ranging from the initial pressure of 10 to 0 Pa. In contrast, the velocity experiences an increase at the stack level, peaking at approximately 1.2 m/s at the position $x = 34.2$ mm.

4.5 Validation of the simulation

A comparative analysis is undertaken to evaluate the accuracy of our numerical model, juxtaposed with the outcomes of Zink et al. [34], who conducted a
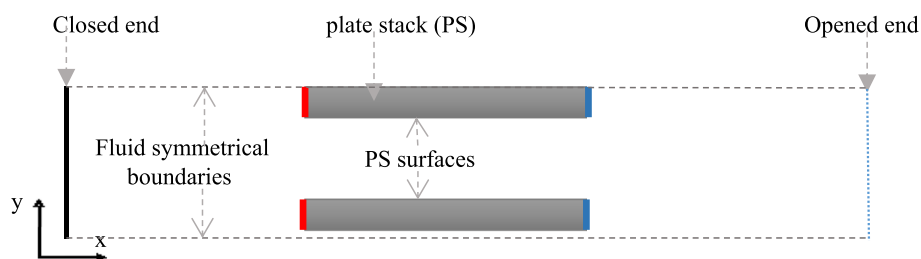

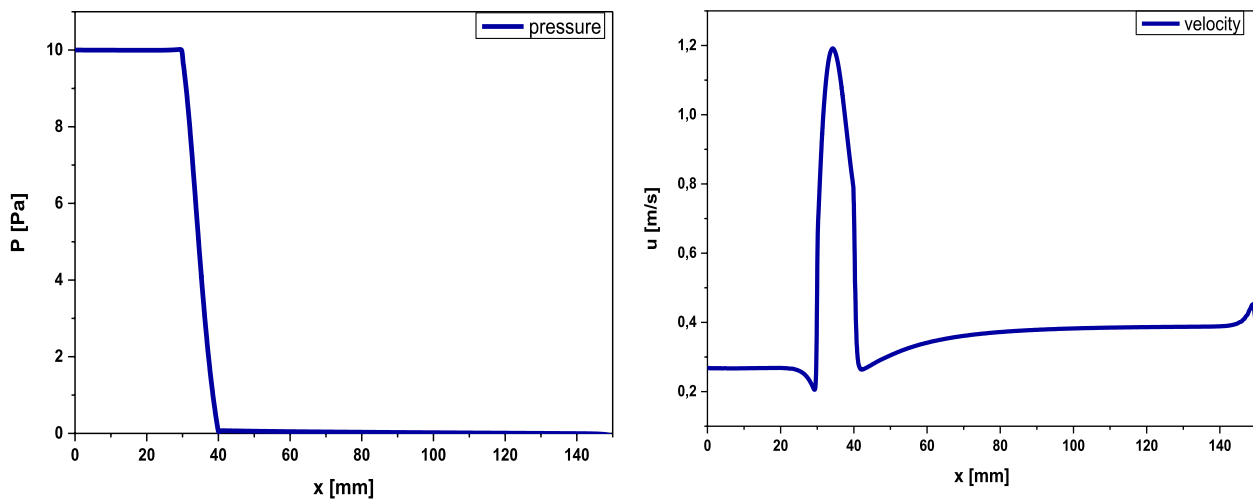**Fig. 8** Different boundaries of the simulation domain

Fig. 9 Initial distribution of the pressure and velocity field along the resonator

computational fluid dynamics (CFD) simulation of a standing-wave engine using Fluent software. Our model adheres to the same precise characteristics and properties applied in Zink et al.'s work. Upon completing the model simulation, spanning from the transition phase of the initial pressure disturbance to the pressure oscillations at steady state (Fig. 10b), and subsequently employing fast Fourier transform (FFT) analysis on the acoustic pressure oscillations (Fig. 10c), the results indicate that the acoustic pressure reached approximately 4694 Pa, with the main operating frequency of the simulated model at about 584 Hz. This frequency aligns with the theoretical operating frequency of a thermoacoustic engine featuring a quarter-wave resonator with a total length of 0.15 m. Comparing the pressure and frequency with the findings reported by [34], there is a difference of 3.83% for the acoustic pressure and 1.35% for the operating frequency. These variances fall within an acceptable range.

5 Results and discussions

The acoustic pressure amplitude and operating frequency stand out as pivotal parameters in gauging the strength of thermoacoustic oscillations, playing a crucial role in propelling any thermoacoustic system. This section is subdivided into six segments: the presentation of simulation results for the model considered as the reference case (as described previously in Sect. 4.1). Furthermore, a comparative analysis is provided, displaying the simulations for various resonator shapes. The graphs depict the time-dependent evolution of acoustic oscillations from the initial disturbance to steady state, enabling a comprehensive comparison of acoustic pressure amplitude and frequency across different scenarios.

5.1 Results obtained for the reference sample

Figures 11 and 12 depict the progression of pressure oscillations at the closed end, fast Fourier transform analysis, acoustical oscillations at the steady state, and the distribution of acoustic pressure based on the length of the thermoacoustic engine, respectively.

The self-excited process of the acoustic wave, generated by imposing a temperature gradient along the stack of parallel plates, is illustrated in Fig. 11, spanning from the initial disturbance to the steady state for the reference sample. The simulations utilize a time step of $1e^{-5}$, encompassing 100 thousand time steps (equivalent to 1 s). The progress of the generated pressure can be delineated into three distinct phases:

- First phase (0–8 ms): In this initial phase, system instability occurs as the temperature gradient at the ends of the stack reaches the imposed gradient at the ends of the plates.
- Second phase (8 ms–0.4 s): The system approaches equilibrium between various energy losses, encompassing viscous and thermal losses to the surrounding environment. The amplitude of the acoustic pressure continues to gradually increase.
- Last phase (0.4 s–steady state): The progress of the acoustic wave, generated by converting thermal energy into acoustic energy, reaches a steady state after heating the stack for around 0.4 s. The pressure stabilizes after approximately 43,000 iterations at an amplitude of 4.6 kPa.

Figure 12b illustrates the distribution of acoustic pressure across the entire device length for a specific segment of the oscillation period (T_p). It is observed that the
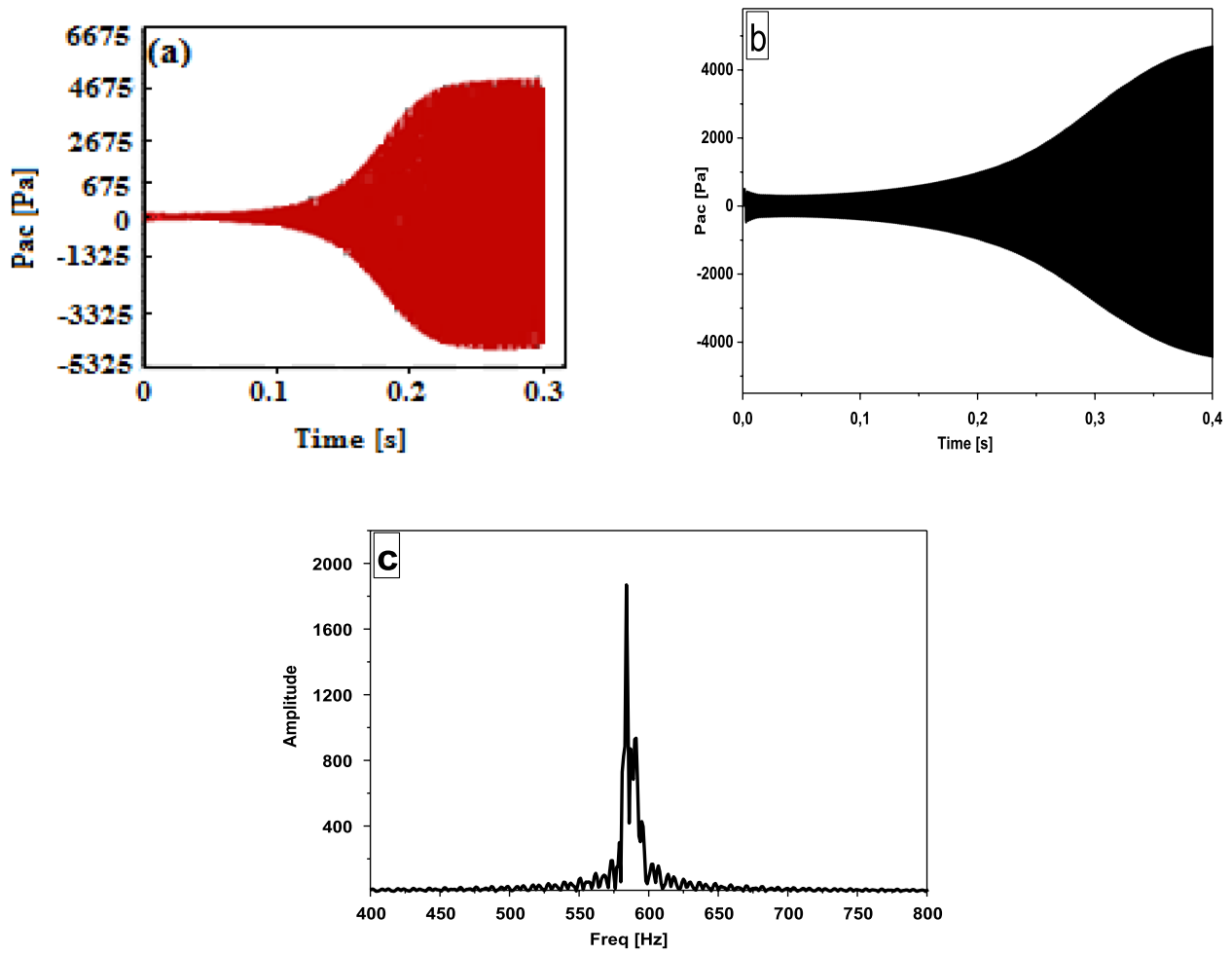
Fig. 10 The evolution of acoustic pressure led by [34] (**a**), found for this study (**b**), and the FFT analysis (**c**)
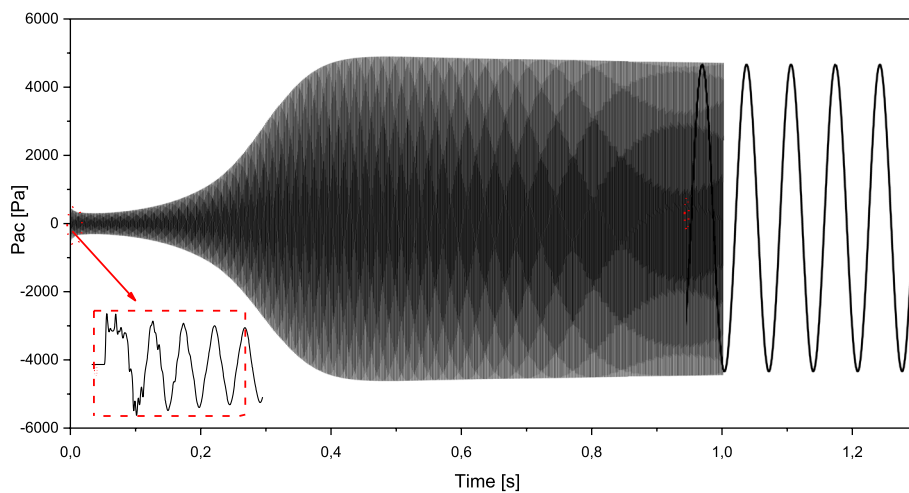

Fig. 11 The process of the acoustic pressure oscillations from the initial disturbance to the steady state
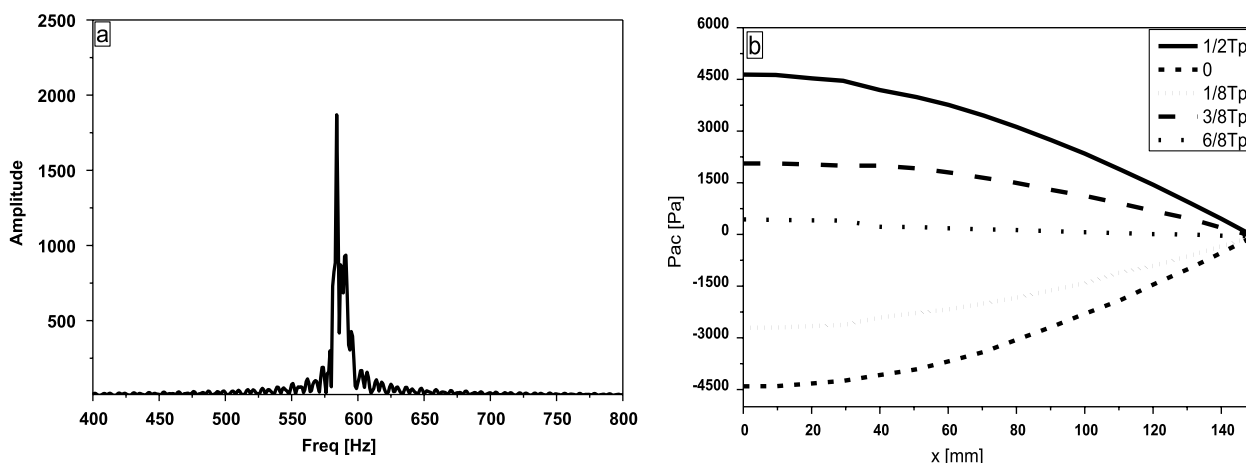
Fig. 12 The FFT analysis (**a**) and the distribution of acoustic pressure depending on the length of TAE (**b**)

closed end of the resonator represents the pressure anti-node, where the pressure amplitude reaches 4.6 kPa, the highest amplitude achieved in this case. Standing-wave self-excited thermoacoustic machines sustain oscillatory motions, converting thermal energy from the hot heat exchanger into generated acoustic power in the stack. The self-excited process unfolds as follows: Initially, the temperature of the cold heat exchanger is set to a low temperature (ambient temperature of 300 K), while the hot heat exchanger is continuously heated to a high temperature of 900 K. The temperature gradient between the ends of the plates increases rapidly. Once this temperature difference reaches the critical gradient, a time-averaged thermodynamic stream is produced beside the stack. Disturbances generated by the heat gradient imposed on the ends of the plates gradually accelerate, overcoming dissipation instigated by the heat exchangers during propagation. These disturbances continuously occur and are amplified by the resonator. FFT analysis of the pressure oscillation (Fig. 12a) reveals a main operating frequency of approximately 585 Hz.

5.2 The self-excited process with different resonator shapes

The evolution of self-excited thermoacoustic oscillations from the initial disturbance to the limit cycle (steady state) and the behavior of the oscillation for various cases—resonator length extension/refraction, tapered resonators, narrowed resonators, curved resonators, and resonators formed of two sections of different diameters—are illustrated in Fig. 13. In this study, twenty-eight tests were conducted to explore the impact of resonator geometry on the performance of a standing-wave thermoacoustic engine. Apart from

the reference case presented earlier, which serves as the baseline, 9 runs were carried out to investigate the impact of resonator extension/refraction, 12 for tapered resonators, 9 for curved resonators, and 5 for resonators of two different diameters. The results are presented graphically in Fig. 13a, b, c, d, and e, respectively, for shapes comparison analysis. For each case studied, Fig. 13 illustrates that the acoustic pressure increases as the temperature gradient is applied along the stack of parallel plates before reaching the steady state. However, the time required to reach the limit-cycle process varies among the cases. Resonator length significantly influences the excitation of the TAE, as evident in Fig. 13a. The time required to reach the limit cycle decreases from approximately 0.6 to 0.3 s when the resonator is extended from 140 to 270 mm, respectively. This suggests a greater input energy requirement to limit viscous losses relative to the wave-guide length. For tapered resonators, there is a distinct difference between the effects of extending the width of the open end (Fig. 13b) and narrowing it (Fig. 13c) on the self-excitation process. Extending the open end increases the time required to reach the limit cycle, whereas narrowing the open end shows a minor difference in the time taken to reach the steady state. In curved resonators, the time taken to achieve the steady state is proportional to the number of bends. More bending results in a longer time to reach the steady state (Fig. 13d). For resonators with two different diameters, Fig. 13e shows that the self-excited process reaches the steady state more quickly for smaller diameters (2, 4, and 6 mm) compared to larger diameters (8, 10, and 12 mm). The self-excited process begins around 0.15 s for smaller diameters and around 0.4 s for larger diameters.
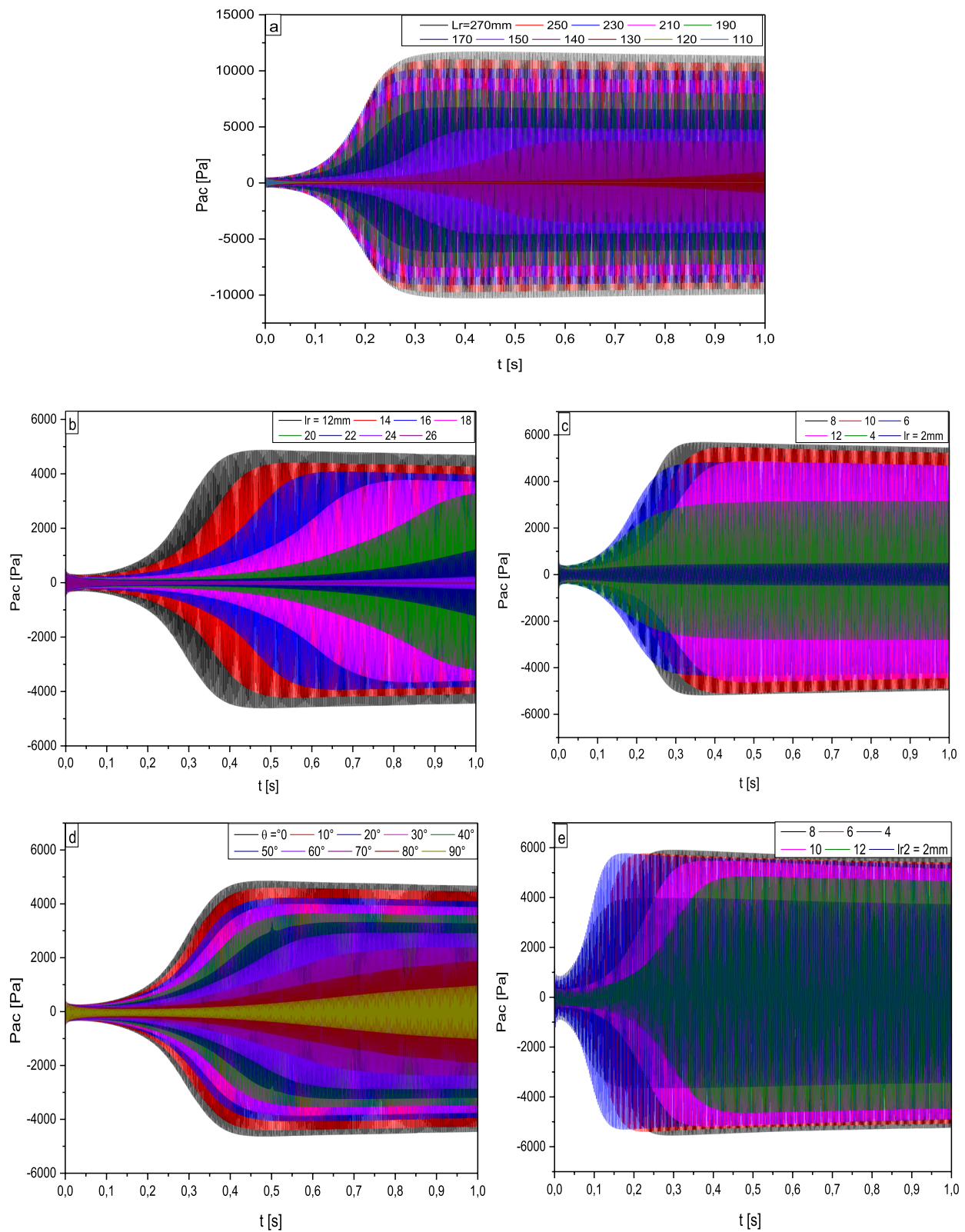
Bouramdane and Bah *Int. J. Air-Cond. Ref.* (2024) 32:4

Page 13 of 22

Fig. 13 Self-excited process of the absolute pressure measured in the right end of the resonator for multiple, **a** length extension/refraction, **b** tapered resonators, **c** narrowed resonators, **d** curved resonators, and **e** the resonator formed of two sections of different diameters

5.3 The acoustic pressure

In order to estimate the amplitude of the acoustic intensities produced by the thermoacoustic engine for each of the five cases of resonator shape studied for multiple values the acoustic pressure amplitude reached at the closed end of the device, expressed in Pa are shown in Fig. 14.

Figure 14a validates the correlation between acoustic pressure and the length of the wave-guide, showcasing a higher pressure amplitude in longer resonators. A notable increase in pressure amplitude, ranging from 960 to 11,660 Pa, is observed as the wave-guide length extends from 130 to 270 mm. It is evident that resonators with a length less than 130 mm do not facilitate the amplification of acoustic pressure, indicating a failure in the process of converting thermal energy into acoustic energy. This outcome aligns with the essential role of the resonator in amplifying the waves generated within the stack. In Fig. 14b, the extension of the open end results in a decrease in acoustic pressure generated by the TAE. A significant drop is observed from 4690 Pa for the straight wave-guide to 35 Pa for the resonator with an extended extremity of 26 mm. Conversely, when the open end is narrowed (Fig. 14c), the pressure amplitude does not strictly follow the length of the open end. Different pressure values are recorded as the open end narrows from 12 to 2 mm, reaching a peak of 5680 Pa at 8 mm and decreasing to 505 Pa at 2 mm. Curved ducts, as illustrated in Fig. 14d, have a detrimental impact on the sound pressure generated by the stack. Increased curvature correlates with a decrease in pressure amplitude, with a drop from 4690 Pa for the straight duct to 980 Pa for the duct curved by 90°. This decline is attributed to acoustic losses resulting from the interaction of the acoustic wave with the resonator walls, where greater curvature expands the interaction zone. In the case of tubes with two parts of different diameters (Fig. 14e), pressure values remain relatively consistent across different diameters. The highest value is 5900 Pa for $d_2 = 8$ mm, followed by $d_2 = 6$ mm, while the smallest value corresponds to a diameter of 2 mm. These results suggest that larger areas and concavities inside the resonator negatively impact wave amplification. This observation aligns with the qualitative interpretation based on the one-dimensional momentum equation for compressible gas:

$$\frac{\partial u}{\partial t} + u \frac{\partial u}{\partial x} = -\frac{1}{\rho} \frac{\partial p}{\partial x} \tag{23}$$

In a TAE, there is typically a nonzero velocity gradient ($\partial u/\partial x \neq 0$) along a standing-wave resonator. For a straight and an iso-diameter wave-guide, the term $\partial u/\partial x$ becomes upper due to an upsurge in the pressure ratio. However, a conical and a curved duct meaningfully reduces the velocity gradient so that this term can be lessened or even neglected and in that way, the thermal and viscous losses are decreased (Tang et al. [11]).

5.4 The operating frequency

Concerning standing-wave devices, optimizing the resonator size is crucial to maximize the quality factor of the acoustic resonance. In this study, simulations were conducted to determine the frequency of the oscillations. The FFT analysis plots for various cases—resonator length extension/refraction, tapered resonators, narrowed resonators, curved resonators, and resonators with two sections of different diameters—using CFD simulation are presented in Fig. 15. Figure 15a illustrates the frequency variations for different resonator lengths, ranging from a short resonator (130 mm) to a long one (270 mm). It is evident that the operating frequency is inversely proportional to the length of the resonator; an increase in length leads to a decrease in the oscillation frequency. For the resonator with a length of 130 mm, the frequency is around 680 Hz, decreasing to approximately 320 Hz for the one with $Lr = 270$ mm. Concerning the width of the ambient side, a larger open end may result in increased frequencies, as depicted in Fig. 15b and c. The resonator with an open end of 2 mm exhibits the lowest frequency, approximately 380 Hz, while the highest frequency, around 700 Hz, is observed for the resonator with an open end of 26 mm. For curved ducts (Fig. 15d), frequency values show an increase, albeit in small proportions, as the curvature of the resonator increases.

In the case of a straight resonator, the frequency measures approximately 584 Hz, and this frequency increases to 655 Hz for a resonator curved by 90°, as illustrated in Fig. 15d. Additionally, Fig. 15e demonstrates that resonators composed of two ducts with different diameters present a potential solution for improved TAE design. The frequency decreases with a reduction in the ambient duct end diameter. The length of the wave-guide mostly fixes resonance frequencies. The equation $f = a/4L$ depicts the link between the resonant frequency (f), resonator length (L), and the sound speed (a) in a quarter-wavelength resonator. An increase in resonator length results in a decrease in resonant frequency. Frequency is a critical parameter in the acoustic field of TAEs, emphasizing the importance of carefully selecting resonator dimensions for optimal operation and higher acoustic power generation. A method to estimate the operating frequencies based on the geometrical parameters of TAEs is proposed by Zhou and Matsubara [35]. Based on the general equation of frequency $f = a/\lambda$, where f is the operating frequency of the TAE, a is the speed of sound which depends on the nature and state of working gasses, and λ is the wavelength which is the distance traveled by the wave during a period of oscillation and the proposed calculation formula is $f = a/nL$,
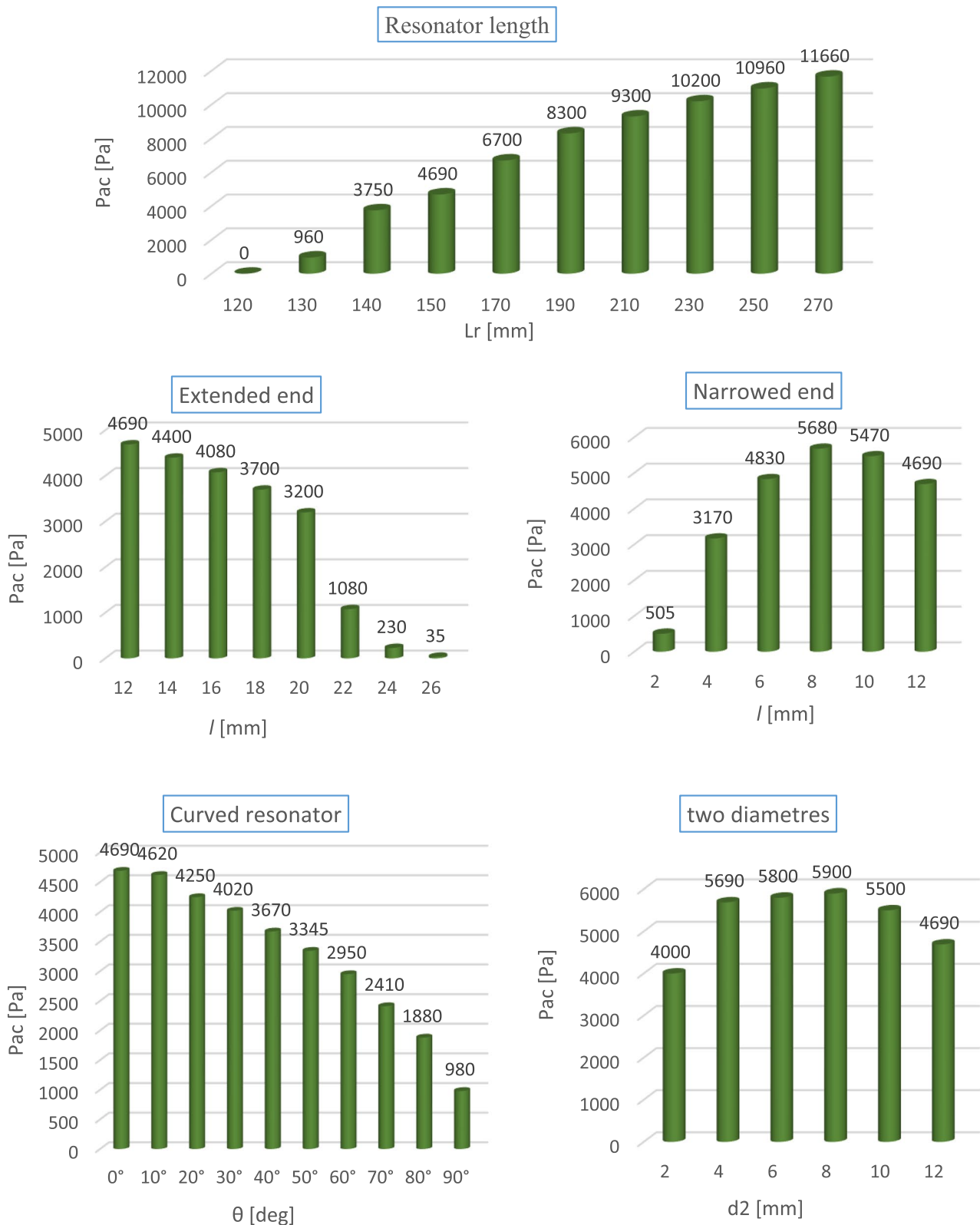
Fig. 14 Acoustic pressure amplitude for multiple, **a** length extension/refraction, **b** tapered resonators, **c** narrowed resonators, **d** curved resonators, and **e** the resonator formed of two sections of different diameters

Fig. 15 Spectrum diagrams obtained through fast Fourier transform (FFT) for different, **a** length extension/refraction, **b** tapered resonators, **c** narrowed resonators, **d** curved resonators, and **e** the resonator formed of two sections of different diameters
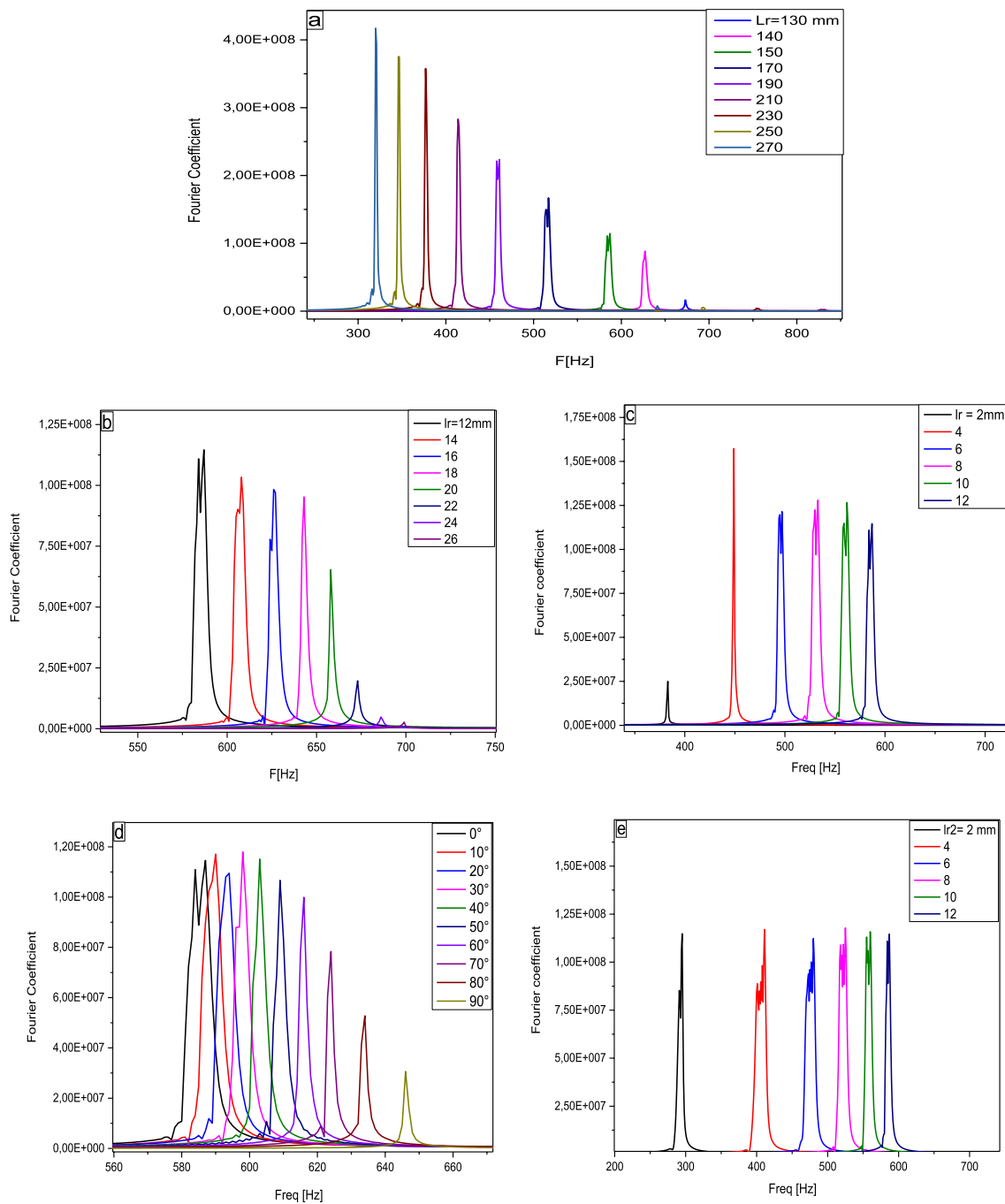
where L is the wave-guide length and n is the acoustic field pattern and depends on the geometry of TAE. If the duct end can be represented by a closed extremity, the oscillation mode of the thermoacoustic system is 1/2 of the wavelength ($n=2$), in this case, the wave-guide is called a half-wavelength resonator. However, if the end of the duct is an open extremity, the oscillation mode is 1/4 of the wavelength ($n=4$) and the wave-guide is called a quarter-wavelength resonator. Therefore, for a fixed configuration and a dimension of TAE, it is possible to change the velocity of sound by varying the nature of working fluids, as the results working frequencies of oscillations changed.

Bouramdane and Bah *Int. J. Air-Cond. Ref.* (2024) 32:4
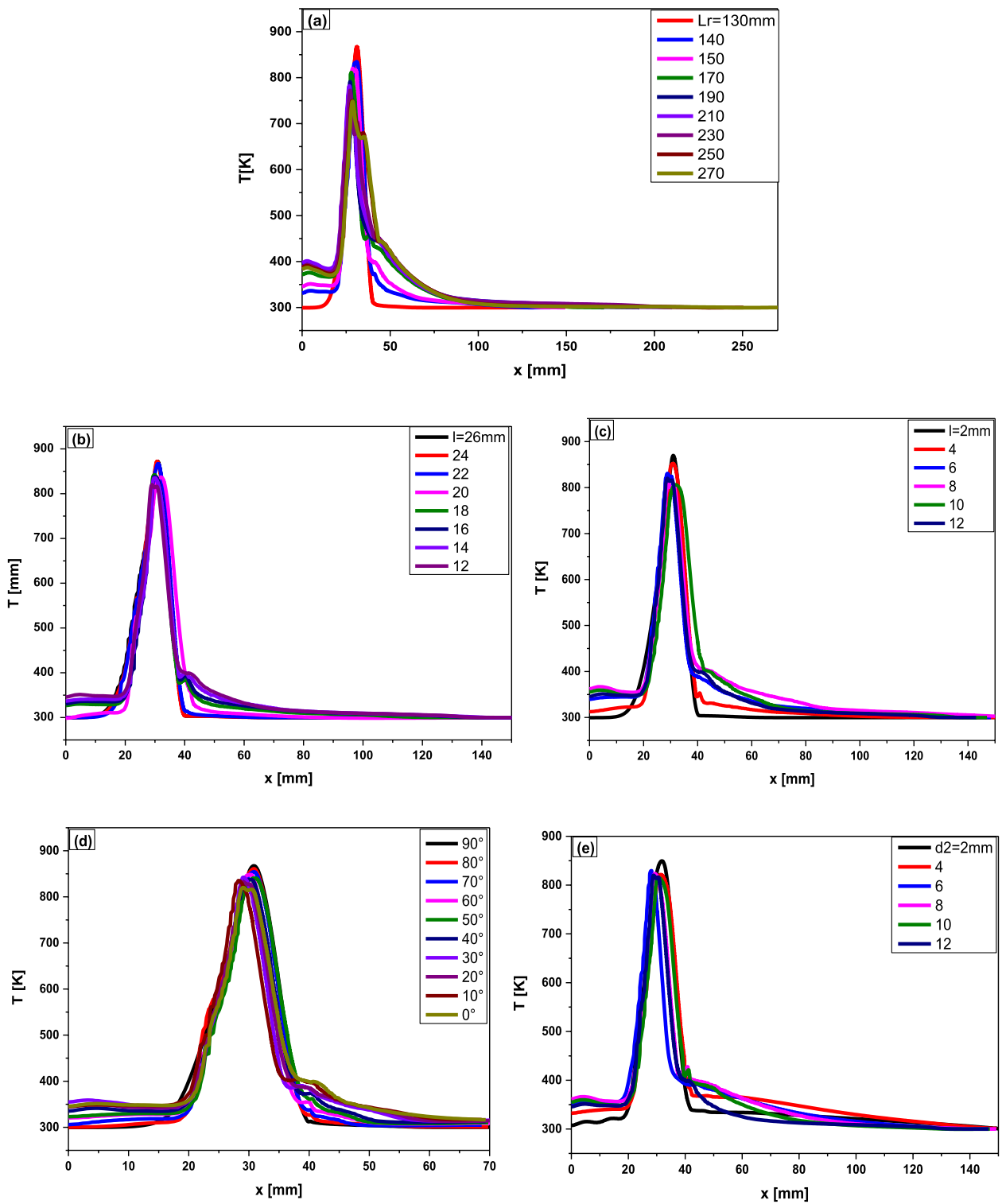
Page 17 of 22

Fig. 16 The temperature along the resonator for different, **a** length extension/refraction, **b** tapered resonators, **c** narrowed resonators, **d** curved resonators, and **e** the resonator formed of two sections of different diameters

Bouramdane and Bah *Int. J. Air-Cond. Ref.* (2024) 32:4

Page 18 of 22

5.5 Temperature along the resonator

The temperature field along the resonator length for various cases, including resonator extension/refraction, tapered resonators, curved resonators, and those formed with two sections of different diameters, is depicted in Fig. 16 using CFD simulation. Before implementing such a model in thermoacoustic devices, understanding the influence of temperature distribution shape on wave amplification and how the resonator shape affects the thermal field around the stack is crucial. Experimental investigations revealed that the acoustic wave amplitude's evolution does not merely correlate with the average temperature gradient at the stack ends. In particular, it is clear that the resonator tend to reduce the temperature difference ($T_h - T_c$) along the stack length as shown in Fig. 16 and summarized in Table 1.

It is noted that the temperature of the cold end (T_c) is proportional to the length of the resonator, T_c increases with the increase in the length of the resonator; it varies from 314 up to 540 K when the length is extended from 130 up to 270 mm. However, this temperature is inversely proportional to the width of the conical resonators; T_c decreases from 400 down to 304 K with the widening of the open end. These results can be explained by the increase in the volume of air in the resonator by the widening of its ambient extremity, which makes the heat exchange between the working fluid and this end increase, which causes a temperature decrease on the cold side of the stack. The same observation is noticed for the curved resonators; the temperature drops from 399 down to 311 K from a right resonator to another curved by 90°. These findings indicate that the resonator shape influences the temperature distribution along the resonator and, notably, in the stack. Moreover, it suggests the possibility of leveraging the resonator's geometry to apply a precise temperature gradient across the stack. While investigations into why and how amplification depends on temperature distribution are yet to be conducted, the constant temperature difference during the self-excited process of the thermoacoustic engine could expedite the establishment of the temperature gradient and facilitate obtaining initial temperatures with different parameters.

5.6 The sound pressure level

While high pressure within thermoacoustic engines is indicative of high efficiency, another critical factor to consider during manufacturing is the sound pressure level (*SPL*) emitted during acoustic wave propagation in a resonator. Figure 17 illustrates the *SPL* for various resonator shapes studied. In Fig. 17a, the *SPL* increases from 153.6 to 175.5 dB as the resonator length extends from 130 to 270 mm. Additionally, *SPL* is inversely proportional to the length of the open end (Fig. 17b), decreasing from 167.5 to 125 dB as the open end lengthens from 12 to 26 mm. Conversely, for narrowed ends, there is an optimum *SPL* value, with the highest observed for an end length of 8 mm and the lowest for 2 mm. For curved resonators, *SPL* values are inversely proportional to the bending angle, decreasing from 167.4 to 153.8 dB for a straight resonator to one curved by 90°. Regarding resonators with two ducts of different diameters, a slight difference in *SPL* values is observed by reducing the second section's diameters from 12 to 2 mm. It is worth noting that the highest reported sound pressure level in the literature is 190 dB, achieved in an advanced traveling-wave engine [36]. These results align with the explanation for the pressure amplitude produced in the resonator, as *SPL* is linked to acoustic pressure by the specific equation:

$$SPL = 20 \log_{10}\left(\frac{P_{ac}}{P_{ref}}\right) [\text{dB}] \tag{24}$$

where P_{ac} is the pressure acoustic reached in the engine, and P_{ref} is the standard reference sound pressure of 20 μPa in the air (the pressure of the smallest sound we can hear $P_{ref} = 2.10^{-5}$ Pa). The *SPL* is expressed in decibel (dB). The human ear can sense pressure variations from 2.10^{-5} to 20 Pa, and sounds producing a sensation beyond this range can be considered unpleasant or annoying. Excessive noise, characterized by a high sound pressure level, can have adverse effects on hearing, causing temporary and partial hearing fatigue or irreversible and debilitating total hearing loss. While noise was initially regarded

Table 1 Cold side temperature for different samples

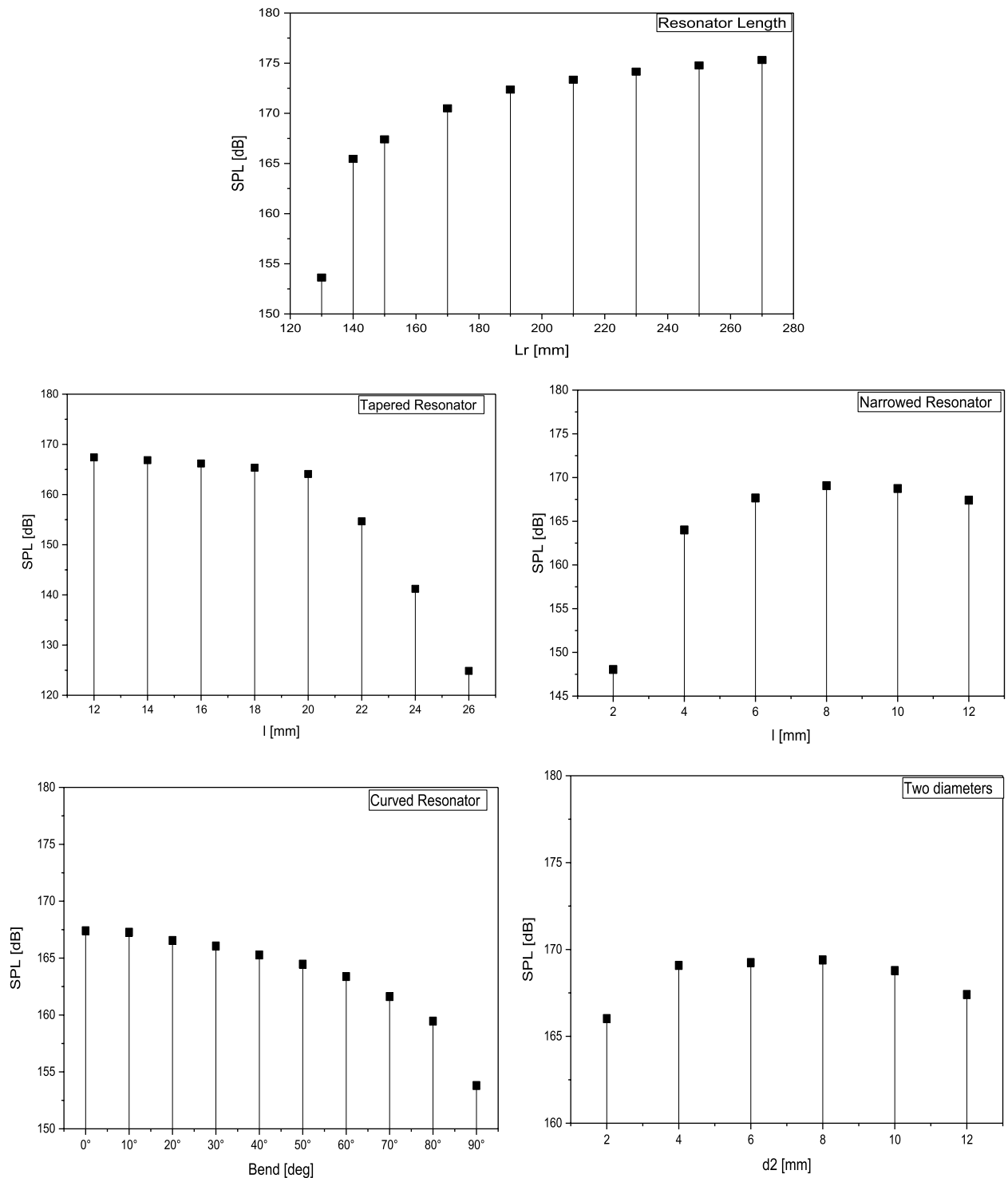| Lr (mm)	T_c (K)	l (mm)	T_c (K)	Bends	T_c (K)	d_2 (mm)	T_c (K)
130	314	10	460	10°	397	2	380
140	374	12	400	20°	390	4	400
150	400	14	398	30°	385	6	395
170	444	16	391	40°	372	8	420
190	450	18	383	50°	360	10	410
210	455	20	370	60°	355	12	399
230	465	22	316	70°	337		
250	530	24	308	80°	315		
270	540	26	304	90°	311		

Fig. 17 Sound pressure level (*SPL*) for different, **a** length extension/refraction, **b** tapered resonators, **c** narrowed resonators, **d** curved resonators, and **e** the resonator formed of two sections of different diameters

as a phenomenon affecting only the auditory system, it has been demonstrated that high sound pressure levels induce reactions involving the entire organism and

surrounding materials. In thermoacoustic devices, it is crucial for the resonator material to possess a large impedance, making the working gas perceive it as a rigid

Bouramdane and Bah *Int. J. Air-Cond. Ref.*   (2024) 32:4

Page 20 of 22

boundary, thus minimizing losses in the acoustic pressure wave. The characteristic impedance of a material is proportional to its density, making dense materials like metals excellent choices for acoustic resonators. Metals, with their high strength-to-weight ratios, also excel as pressure vessels in thermoacoustic applications.

6 Conclusion

Thermoacoustic devices, renowned for converting thermal energy into acoustic energy and vice versa, stand out for their absence of moving mechanical parts, robustness, and environmental friendliness. Despite their simplicity, designing and constructing these machines pose significant technical challenges for researchers. This study employs numerical modeling, specifically CFD simulations using COMSOL Multiphysics, to analyze the dissipation of acoustic energy in the resonator and predict the behavior of a standing-wave thermoacoustic engine, accounting for variations in resonator length and shape. A 2D simulation model is implemented to visualize the temporal evolution of the acoustic wave excitation process and assess engine performance in terms of acoustic pressure, oscillation frequency, temperature distribution along the resonator, and sound pressure level. The study encompasses 28 simulated samples, including the reference case, exploring resonator length extensions/refractions, tapered resonators, curved resonators, and resonators with two ducts of different diameters. Key findings can be summarized as follows: Energy dissipation in the resonator (W_{loss}) increases with the resonator's diameter, and it is proportional to the drive ratio (DR), Prandtl number (Pr), and thermal penetration depth (δ_k). Higher values of DR, Pr, and δ_k lead to increased W_{loss}. CFD analysis reveals that long resonators exhibit higher acoustic pressure amplitudes compared to shorter ones. Tapered resonators produce the highest pressure, with $lr=8$ mm increasing pressure by 17.42%. In curved resonators, pressure amplitude decreases with the angle bend, dropping by 79.1% for a $\theta=90°$ resonator compared to a straight one. Resonators with two different diameters demonstrate the capability to generate large pressure amplitudes (resonator with $d_2=8$ mm producing 20.5% more acoustic pressure than the iso-diameter resonator) with minimized frequencies, reducing viscous and thermal losses. This performance analysis serves as an initial step toward developing a standing-wave thermoacoustic refrigerator powered by a standing-wave thermoacoustic engine. While resonator geometry undeniably influences thermoacoustic device performance, this study lays the foundation for future publications aimed at identifying the most efficient resonator shape for designing a thermally driven thermoacoustic refrigerator model.

7 Nomenclature

a Speed of sound, m·s^{-1}
CFD Computational fluid dynamic
cp Isobaric heat capacity, J·kg^{-1}·K^{-1}
d Diameter, m
DR Drive ratio
F Resonant frequency, Hz
FFT Fast Fourier transform
K Thermal conductivity, W·m^{-1}·K^{-1}
L Length, m
l Large, m
p Pressure amplitude, Pa
P_{ab} Absolute pressure, Pa
P_{ac} Acoustic pressure, Pa
Pr Prandtl number
Rs Gas ideal constant, J·K^{-1}·mol^{-1}
r_{hr} Hydraulic radius, m
S Resonator area, m^2
SPL Sound pressure level, dB
T Temperature, K
TAE Thermoacoustic engine
TAEs Thermoacoustic engines
T_p Time period of one acoustical oscillation, s
∇T Temperature gradient, K·m^{-1}
u Velocity amplitude, m·s^{-1}
W Energy losses, w

7.1 Greek symbols

α Thermal diffusivity, m^2 s
ν Kinematic viscosity, m^2 s
γ Ratio of specific heat
δ_k Thermal penetration depth, m
δ_v Viscous penetration depth, m
λ Wavelength, m
μ Dynamic viscosity, kg m^{-1} s^{-1}
ρ Density, kg m^{-3}
θ Angle of curvature
ω Angular frequency, rad s^{-1}

7.2 Subscripts, superscripts

c Cold
h Hot
$loss$ Losses
m Mean
n Normalized
p Pressure
r Resonator
v Viscous

Authors' contributions
Zahra Bouramdane: Software, Data curation, Formal analysis, Writing the original draft, results interpretation and analysis. Abdellah Bah: Work Supervision,

Bouramdane and Bah *Int. J. Air-Cond. Ref.* (2024) 32:4

Page 21 of 22

Results interpretation and analysis. The author(s) read and approved the final manuscript.

Availability of data and materials

All data generated or analyzed during this study are included in this published article.

Declarations

Competing interests

The authors declare that they have no competing interests.

References

1. Rott N. The heating effect connected with non-linear oscillations in a resonance tube. 1974. https://doi.org/10.1007/BF01596123.
2. Muzzerall, M., Atchley, A. A., & Hofler, T. J. (1987). Acoustically generated temperature gradients in plates. *The Journal of the Acoustical Society of America,82*(S1), S21–S21. https://doi.org/10.1121/1.2024704
3. Swift, G. W. (1992). Analysis and performance of a large thermoacoustic engine. *The Journal of the Acoustical Society of America,92*(3), 1551–1563. https://doi.org/10.1121/1.403896
4. Gaitan, D. F., & Atchley, A. A. (1993). Finite amplitude standing waves in harmonic and anharmonic tubes. *The Journal of the Acoustical Society of America,93*(5), 2489–2495. https://doi.org/10.1121/1.405870
5. Lawrenson, C. C., Lipkens, B., Lucas, T. S., Perkins, D. K., & Doren, T. W. V. (1998). Measurements of macrosonic standing waves in oscillating closed cavities. *The Journal of the Acoustical Society of America,104*(2), 623. https://doi.org/10.1121/1.423306
6. Ilinskii, Y. A., Lipkens, B., Lucas, T. S., Van Doren, T. W., & Zabolotskaya, E. A. (1998). Nonlinear standing waves in an acoustical resonator. *The Journal of the Acoustical Society of America,104*(5), 2664–2674. https://doi.org/10.1121/1.423850
7. Chun, Y.-D., & Kim, Y.-H. (2000). Numerical analysis for nonlinear resonant oscillations of gas in axisymmetric closed tubes. *The Journal of the Acoustical Society of America,108*(6), 2765–2774. https://doi.org/10.1121/1.1312363
8. Hamilton, M. F., Ilinskii, Y. A., & Zabolotskaya, E. A. (2001). Linear and nonlinear frequency shifts in acoustical resonators with varying cross sections. *The Journal of the Acoustical Society of America,110*(1), 109–119. https://doi.org/10.1121/1.1379080
9. Yu, Z. B., Li, Q., Chen, X., Guo, F. Z., & Xie, X. J. (2005). Experimental investigation on a thermoacoustic engine having a looped tube and resonator. *Cryogenics,45*(8), 566–571. https://doi.org/10.1016/j.cryogenics.2005.06.007
10. Luo, E. C., Ling, H., Dai, W., & Yu, G. Y. (2006). Experimental study of the influence of different resonators on thermoacoustic conversion performance of a thermoacoustic-Stirling heat engine. *Ultrasonics,44*, e1507–e1509. https://doi.org/10.1016/j.ultras.2006.08.008
11. Tang, K., Chen, G. B., Jin, T., Bao, R., & Li, X. M. (2006). Performance comparison of thermoacoustic engines with constant-diameter resonant tube and tapered resonant tube. *Cryogenics,46*(10), 699–704. https://doi.org/10.1016/j.cryogenics.2006.04.006
12. Bao, R., Chen, G., Tang, K., Jia, Z., & Cao, W. (2006). Influence of resonance tube geometry shape on performance of thermoacoustic engine. *Ultrasonics,44*, e1519–e1521. https://doi.org/10.1016/j.ultras.2006.08.005
13. Xie, X., Li, Q., Li, Z., & Li, Q. (2006). Investigation on the different types of resonators in the thermoacoustic Stirling prime mover. *Ultrasonics,44*, e1503–e1505. https://doi.org/10.1016/j.ultras.2006.08.003
14. Ueda, Y., & Kato, C. (2008). Stability analysis of thermally induced spontaneous gas oscillations in straight and looped tubes. *The Journal of the Acoustical Society of America,124*(2), 851–858. https://doi.org/10.1121/1.2939134
15. Zink, F., Vipperman, J., & Schaefer, L. (2010). CFD simulation of a thermoacoustic engine with coiled resonator. *International Communications in Heat and Mass Transfer,37*(3), 226–229. https://doi.org/10.1016/j.icheatmasstransfer.2009.09.001
16. Hariharan, N. M., Sivashanmugam, P., & Kasthurirengan, S. (2012). Influence of stack geometry and resonator length on the performance of thermoacoustic engine. *Applied Acoustics,73*(10), 1052–1058. https://doi.org/10.1016/j.apacoust.2012.05.003
17. Qiu, L. M., Lai, B. H., Li, Y. F., & Sun, D. M. (2012). Numerical simulation of the onset characteristics in a standing wave thermoacoustic engine based on thermodynamic analysis. *International Journal of Heat and Mass Transfer,55*(7), 2200–2203. https://doi.org/10.1016/j.ijheatmasstransfer.2011.11.043
18. Hariharan, N. M., Sivashanmugam, P., & Kasthurirengan, S. (2013). Effect of resonator length and working fluid on the performance of twin thermoacoustic heat engine – Experimental and simulation studies. *Computers & Fluids,75*, 51–55. https://doi.org/10.1016/j.compfluid.2013.01.019
19. Muralidharan, H., Hariharan, N. M., Perarasu, V. T., Sivashanmugam, P., & Kasthurirengan, S. (2013). Computational fluid dynamics simulation of open ended thermoacoustic prime mover with straight and tapered resonator. *HVAC&R Research,19*(3), 208–212. https://doi.org/10.1080/10789669.2012.755897
20. Yang, D. K. W., Abakr, Y. A., & Ghazali, N. M. (2013). Experimental investigations on the effects of coiling and bends on the sound energy losses through a resonator tube. *Procedia Engineering,56*, 842–848. https://doi.org/10.1016/j.proeng.2013.03.205
21. Tourkov, K., Zink, F., & Schaefer, L. (2015). Thermoacoustic sound generation under the influence of resonator curvature. *International Journal of Thermal Sciences,88*, 158–163. https://doi.org/10.1016/j.ijthermalsci.2014.09.016
22. Cahyadi, D., Adhitama, Y., Setiawan, I., & Utomo, A. (2017). Experimental study of resonance frequency at prime mover thermoacoustic standing wave. *Journal of Physics: Theories and Applications,1*, 157. https://doi.org/10.20961/jphystheor-appl.v1i2.19316
23. Yang, D., Sogaro, F. M., Morgans, A. S., & Schmid, P. J. (2019). Optimising the acoustic damping of multiple Helmholtz resonators attached to a thin annular duct. *Journal of Sound and Vibration,444*, 69–84. https://doi.org/10.1016/j.jsv.2018.12.023
24. Bourquard, C., & Noiray, N. (2019). Stabilization of acoustic modes using Helmholtz and quarter-wave resonators tuned at exceptional points. *Journal of Sound and Vibration,445*, 288–307. https://doi.org/10.1016/j.jsv.2018.12.011
25. Bouramdane, Z., Bah, A., Martaj, N., Alaoui M. (2019). Thermoacoustic effect under the influence of resonator curvature. In: Hajji B, Tina GM, Ghoumid K, Rabhi A, Mellit A, eds., *Proceedings of the 1st international conference on electronic engineering and renewable energy*. In. Lecture notes in electrical engineering. Springer. pp. 164–169.
26. Balonji, S., Alcock, A. C., Tartibu, L. K., & Jen, T. C. (2019). Performance alteration of standing-wave thermoacoustically-driven engine through resonator length adjustment. *Procedia Manufacturing,35*, 1350–1355. https://doi.org/10.1016/j.promfg.2019.09.002
27. Harikumar, G., Ho, K. H., Wang, K., Dubey, S., & Duan, F. (2019). Thermoacoustic energy conversion in a square duct. *Energy Procedia,158*, 1811–1816. https://doi.org/10.1016/j.egypro.2019.01.425
28. Swift, G. W. (1988). Thermoacoustic engines. *The Journal of the Acoustical Society of America,84*(4), 1145–1180. https://doi.org/10.1121/1.396617
29. Olson, J. R., & Swift, G. W. (1994). Similitude in thermoacoustics. *The Journal of the Acoustical Society of America,95*(3), 1405–1412. https://doi.org/10.1121/1.408581
30. COMSOL Multiphysics Reference Manual. p. 1742. https://www.comsol.fr/.
31. Bouramdane, Z., Bah, A., Alaoui, M., & Martaj, N. (2023). Design optimization and CFD analysis of the dynamic behavior of a standing wave thermoacoustic engine with various geometry parameters and boundary conditions. *International Journal of Air-Conditioning and Refrigeration,31*, 1. https://doi.org/10.1007/s44189-022-00018-0
32. Bouramdane, Z., Bah, A., Alaoui, M., & Martaj, N. (2022). Numerical analysis of thermoacoustically driven thermoacoustic refrigerator with a stack of parallel plates having corrugated surfaces. *International Journal of Air-Conditioning and Refrigeration,30*, 1. https://doi.org/10.1007/s44189-022-00002-8
33. Bouramdane, Z., Bah, A., Alaoui, M., Martaj, N. (2021). CFD modeling and performance analysis of a thermoacoustically driven thermoacoustic refrigerator. *International Journal of Air-Conditioning and Refrigeration*. 2150029. https://doi.org/10.1142/S2010132521500292.

34. Zink, F., Vipperman, J., Schäfer L. (2008). *Advancing thermoacoustics through CFD simulation using fluent*, vol. 8. https://doi.org/10.1115/IMECE2008-66510.

35. Zhou, S., & Matsubara, Y. (1998). Experimental research of thermoacoustic prime mover. *Cryogenics,38*, 813–822. https://doi.org/10.1016/S0011-2275(98)00055-1

36. Garrett, S. L. (1999). Reinventing the engine. *Nature,399*(6734), 303–305. https://doi.org/10.1038/20546

Publisher's Note

Springer Nature remains neutral with regard to jurisdictional claims in published maps and institutional affiliations.